Callosal fiber length scales with brain size according to functional lateralization, evolution, and development

Abbreviated title: Callosal fiber length scaling

Liyuan Yang[1], Chenxi Zhao[1], Yirong Xiong[1], Suyu Zhong[1], Di Wu[1], Shaoling Peng[1], Michel Thiebaut de Schotten[2, 3], Gaolang Gong[1, 4, 5*]

[1] State Key Laboratory of Cognitive Neuroscience and Learning & IDG/McGovern Institute for Brain Research, Beijing Normal University, Beijing, China

[2] Brain Connectivity and Behaviour Laboratory, Sorbonne Universities, Paris, France

[3] Groupe d'Imagerie Neurofonctionnelle, Institut des Maladies Neurodégénératives-UMR 5293, CNRS, CEA, University of Bordeaux, Bordeaux, France

[4] Beijing Key Laboratory of Brain Imaging and Connectomics, Beijing Normal University, Beijing, China

[5] Chinese Institute for Brain Research, Beijing, China

*** Correspondence:** Dr. Gaolang Gong E-mail: gaolang.gong@bnu.edu.cn

Conflict of interest: The authors declare no competing financial interests.

Acknowledgments

We thank Yanchao Bi for valuable discussions. This work was supported by the National Science Foundation of China [8217071142, 82021004, G.G.]. Michel Thiebaut de Schotten has received funding from the European Research Council (ERC) under the European Union's Horizon 2020 research and innovation programme (grant agreement no. 818521). Data were provided by the Human Connectome Project, WU-Minn Consortium (Principal Investigators: David Van Essen and Kamil Ugurbil; 1U54MH091657) funded by the 16 NIH Institutes and Centers that support the NIH Blueprint for Neuroscience Research; and by the McDonnell Center for Systems Neuroscience at Washington University. UK Biobank brain imaging was funded by the UK Medical Research Council and the Wellcome Trust.

Abstract

Brain size significantly impacts the organization of white matter fibers. Fiber length scaling – the degree to which fiber length varies according to brain size – was overlooked. We investigated how fiber lengths within the corpus callosum, the most prominent white matter tract, vary according to brain size. The results showed substantial variation in length scaling among callosal fibers, replicated in two large healthy cohorts (~2000 individuals). The underscaled callosal fibers mainly connected the precentral gyrus and parietal cortices, whereas the overscaled callosal fibers mainly connected the prefrontal cortices. The variation in such length scaling was biologically meaningful: larger scaling corresponded to larger neurite density index but smaller fractional anisotropy values; cortical regions connected by the callosal fibers with larger scaling were more lateralized functionally as well as phylogenetically and ontogenetically more recent than their counterparts. These findings highlight an interaction between interhemispheric communication and organizational and adaptive principles underlying brain development and evolution.

Significance Statement

Brain size varies across evolution, development, and individuals. Relative to small brains, the neural fiber length in large brains is inevitably increased, but the degree of such increase may differ between fiber tracts. Such a difference, if it exists, is valuable for understanding adaptive neural principles in large versus small brains during evolution and development. The present study showed a substantial difference in the length increase between the callosal fibers that connect the two hemispheres, replicated in two large healthy cohorts. Altogether, our study demonstrates that reorganization of interhemispheric fibers length according to brain size is intrinsically related to fiber composition, functional lateralization, cortical myelin content, evolutionary and developmental expansion.

Introduction

Total brain size varies dramatically across evolution, development, and individuals. Large brains' structures are not simple linearly scaled versions of small brains, e.g., cortical expansion of large brains is disproportionately larger for higher cognitive function regions (Hill et al., 2010; Reardon et al., 2018). The scaling patterns of specific brain structures provide essential clues for understanding organizational and adaptive principles underlying brain development and evolution (Zhang and Sejnowski, 2000; Herculano-Houzel et al., 2010; Van Essen, 2018).

An increase in brain size also has a significant impact on brain circuits (Kaas, 2000). In larger brains, fiber length is inevitably increased, accompanied by a longer delay in conduction and slower information transfer. It is well known that brain fibers can increase their myelination and diameter to increase conduction velocity and compensate for this delay (Waxman et al., 1995; Wang et al., 2008). These adaptations, however, cannot apply systematically to all fiber tracts due to the limit in brain space and energy consumption (Ringo et al., 1994), leading to alternative biological strategies that might impact fiber length differently. While the fiber length adjustment to brain size has been assumed uniform so far, heterogeneity in fiber length scaling may reveal adaptive principles underlying brain development and evolution.

In the present study, we assessed whether length scaling variations exist according to brain size within the corpus callosum (CC), the principal white matter (WM) bundle supporting the communication between the two brain hemispheres. We further investigated the relationship between CC length scaling with fiber composition, functional lateralization, cortical myelin content, and cortical evolutionary and developmental expansion.

Materials and Methods

Discovery dataset

The discovery dataset included all possible Human Connectome Project (HCP) participants for whom both diffusion and T1 images were available (Van Essen et al., 2012). It comprised 928 healthy young adults (female/male: 503/425; age range: 22-37 years). Retest diffusion and T1 imaging data were available on 35 of these subjects (test-retest interval: 1 month - 11 months). Informed consent was obtained from all subjects, and the protocol was approved by the Institutional Review Board of Washington University. Magnetic resonance imaging (MRI) scanning was performed using a customized Siemens Connectome Skyra 3T scanner. Diffusion-weighted (DW) images were acquired using a spin-echo echo-planar imaging (EPI) sequence with the following parameters: repetition time (TR) = 5520 ms, echo time (TE) = 89.5 ms, flip angle = 78°, field of view (FOV) = 210 × 180 mm^2, matrix = 168 × 144, slices = 111, and resolution = 1.25 mm × 1.25 mm × 1.25 mm. Diffusion weightings of b = 0, 1000, 2000, and 3000 s/mm^2 were applied in 18, 90, 90 and 90 directions, respectively. High-resolution 3D T1-weighted (T1W) images were acquired using a magnetization prepared rapid gradient echo (MPRAGE) sequence and the following parameters: TR = 2400 ms, TE = 2.14 ms, TI = 1000 ms, flip angle = 8°, FOV = 224 × 224 mm^2, and resolution = 0.7 mm × 0.7 mm × 0.7 mm. DW and T1W images were preprocessed using the HCP minimal preprocessing pipeline (Glasser et al., 2013).

Replication dataset

A subset of the UK Biobank (UKB) dataset was selected as our replication dataset (Miller et al., 2016). To maximally match the age range and sample size with the discovery dataset, all UKB participants under the age of 43 years for whom both diffusion and T1

images were available were included in the replication dataset, comprising 981 healthy adults (female/male: 562/419; age range: 40-43 years). Informed consent was obtained from all UKB subjects, and the protocol was approved by the North West Multicenter Research Ethics Committee. MRI data from the UKB sample were acquired using a Siemens Skyra 3T scanner. DW images were acquired using a spin-echo EPI sequence with the following parameters: TR = 3600 ms, TE = 92 ms, flip angle = 78°, FOV = 208 × 208 mm^2, 72 slices, and resolution = 2 mm × 2 mm × 2 mm. Diffusion weightings of b = 0, 1000, 2000 s/mm^2 were applied in 5, 50, and 50 directions. High-resolution 3D T1W images were acquired using an MPRAGE sequence and the following parameters: TR = 2000 ms, TE = 2.01 ms, TI = 880 ms, flip angle = 8°, FOV = 256 × 256 mm^2, and resolution = 1 mm × 1 mm × 1 mm. DW and T1W images were preprocessed using the UKB brain imaging processing pipeline (Alfaro-Almagro et al., 2018).

Total brain size

The brain size was defined as the total brain volume (TBV). Specifically, the T1W image of each individual was segmented into gray matter (GM), WM, and cerebrospinal fluid (CSF) using the FAST tool of the FMRIB Software Library (FSL) (Smith et al., 2004). The TBV was then calculated as the sum of WM and GM volume.

Individual midsagittal CC (mCC) and its alignment to the template

The HCP minimal preprocessing pipeline aligned the anterior commissure (AC), AC–posterior commissure (PC) line, and interhemispheric plane of the T1W images to the MNI template using a rigid transform of 6 degrees of freedom. This transform maintains the original size and shape of the brain. We applied the same aligning procedure to the T1W images of UKB participants. On the resultant T1W image of each individual, the

96 midsagittal plane's sagittal slice was selected, and the midsagittal CC (mCC) boundary was
97 then manually outlined by a trained rater (D.W). The mCC boundary of 50 randomly
98 selected participants was outlined two weeks later by the rater to assess the manual
99 outlining reliability. The Dice coefficient of the mCC masks ranged from 0.95 to 0.99
100 (mean: 0.98, STD: 0.009), and the intraclass correlation coefficient (ICC) of the mCC area
101 reached 0.99.

102 To ensure voxel-wise comparability across individuals, the individual mCC was
103 nonlinearly aligned to a template mCC in MNI space, which was manually outlined on the
104 MNI152 template image. Specifically, the 2D sagittal image of the template mCC was set
105 as the target image (or the fixed image), and the 2D sagittal image of the individual mCC
106 was set as the source image (or the moving image). The two 2D images were first smoothed
107 with a 2D Gaussian smoothing kernel (sigma = 1) by using the 'imgaussfilt' function in
108 MATLAB. First, we linearly aligned the source image to the target image (i.e., performed
109 a 2D affine transform of 8 degrees of freedom, including translation, rotation, scaling, and
110 shearing) using the 'imregtform' function in MATLAB. Next, we performed nonlinear
111 registration from the linearly aligned source image to the target image using the demons
112 algorithm that was implemented by the 'imregdemons' function in MATLAB (Thirion,
113 1998; Vercauteren et al., 2009). Here, three multiresolution image pyramid levels were
114 used, and 100 iterations were estimated at each pyramid level. Gaussian smoothing (sigma
115 = 1) was applied to regularize the accumulated displacement field at each iteration. To
116 maximize the aligning accuracy, this whole nonlinear registration procedure was iterated 5
117 times. Finally, the linear and nonlinear displacement fields were successively applied to

118 transform the individual mCC to the template space with linear interpolation. For each
119 individual, the mCC alignment was carefully checked by visual inspection.

120 **Callosal fiber length**

121 Diffusion magnetic resonance imaging (dMRI) tractography was used to extract
122 callosal fiber streamlines passing through the mCC. First, fiber orientation distributions
123 (FODs) of each voxel were estimated using multishell, multitissue constrained spherical
124 deconvolution with a harmonic order of 8 and default parameters (Tournier et al., 2007;
125 Jeurissen et al., 2014). Probabilistic fiber tracking was then performed using the 2nd-order
126 integration over FODs (iFOD2) algorithm in Mrtrix3 (Tournier et al., 2019). Given our
127 focus on callosal fibers, the mCC was set as an inclusion mask (i.e., saving only fibers
128 traversing the mCC) in fiber tracking. Due to the ambiguous existence of callosal fibers
129 connecting bilateral subcortical nuclei, all subcortical nuclei were set as exclusion masks
130 (i.e., fibers traversing them were discarded). Here, subcortical nuclei, including the
131 thalamus, hippocampus, amygdala, caudate, putamen, palladium, and accumbens, were
132 extracted using the FIRST tool of the FSL (Smith et al., 2004). To improve the biological
133 accuracy of the tractograms, the anatomically constrained tractography (ACT) framework
134 was used, which incorporates prior anatomical information into the tractography (Smith et
135 al., 2012). The anatomical information was obtained by segmenting T1W images into
136 tissue partial volume maps (PVMs) for WM, GM, and CSF using the FSL tools. The
137 resultant PVM images were then taken as anatomical priors into the ACT framework. For
138 the HCP participants, the minimal preprocessed T1W images were well aligned with the
139 DW images; therefore, the mCC and PVM images were already in the DW image space.
140 For each UKB participant, we linearly aligned the fractional anisotropy (FA) image to the

141 T1W images, and the inverted transform was then used to convert the mCC and PVM
142 images to the DW image space. The detailed fiber-tracking parameters were as follows:
143 step size = 0.625 mm (default), maximum curvature per step = 45°, FOD threshold = 0.05,
144 and length range = 2.5-250 mm. For each subject, 10 million streamlines were generated
145 by seeding from and ending into the ACT-generated GM-WM interface (GMWMI). For
146 the UKB participants, the generated tractograms in the DW image space were transformed
147 back into the T1W image space.

148 For each mCC voxel, the streamlines passing through it and linking the bilateral
149 cerebral cortex were selected. Their average length was computed as the callosal length
150 value for this voxel. One mCC map of fiber length was obtained for each subject, which
151 was further transformed into the standard mCC template space described above. To
152 evaluate the test-retest reproducibility of the voxel-wise measure for callosal fiber length,
153 we reran the above analyses for the 35 HCP retest subjects with their retest diffusion and
154 T1 imaging data (test-retest interval: 1 month - 11 months). For each mCC voxel, ICC was
155 then calculated for the fiber length measure using the test-retest data.

156 **Length scaling coefficients with brain size**

157 As was done previously (Reardon et al., 2018), we estimated the fiber length scaling
158 coefficient with greater brain size using a multiple regression model: *log* (fiber length) = β
159 * *log* (brain size) + β_1* age + β_2* sex + intercept, where the β represents the length scaling
160 coefficient. In the model, age and sex were included as covariates. This regression model
161 fitting was applied to each voxel of the mCC template, resulting in a mCC map for the
162 callosal fiber length scaling coefficient (Fig. 1).

163 Theoretically, if WM fibers' internal geometrical shape is invariant for brain size, the
164 WM fiber length should scale as the 1/3 power of brain size. In this case, the proportional
165 relationship between the two measures, one in 1-dimension and the other in 3-dimension,
166 is preserved during scaling. This is referred to as the isometric scaling or iso-scaling. For
167 empirical scaling coefficients, coefficients > 1/3 indicate that the WM fiber length scales
168 more with greater brain size, i.e., over-scaling; coefficients < 1/3 indicate that WM fiber
169 length scales less with brain size, i.e., under-scaling. Each voxel's scaling coefficient on
170 the mCC template was statistically compared to 1/3 to identify the significant clusters with
171 over-scaling or under-scaling. To correct for multiple comparisons, the false discovery rate
172 (FDR) procedure was performed at q value of 0.05 (Genovese et al., 2002).

173 **Validation analysis of callosal tractography**

174 The validity of our callosal tractography is critical for measuring callosal fiber length
175 and performing subsequent length scaling analyses. To validate our callosal tractography
176 results, we evaluated a set of characteristics of tractography-based callosal connections as
177 following.

178 First, we selected several cortical regions of interest (ROIs) that showed length under-
179 scaling and over-scaling in scaling analyses, and investigated how tightly their callosal
180 streamlines are clustered on the mCC and how the clusters on the mCC correspond with
181 previous anatomical studies. Specifically, we extracted the cortical ROIs using the
182 HCPMMP atlas (Glasser et al., 2016). The selected ROIs included 1) area 4 on the primary
183 motor cortex, 2) area 2 on the somatosensory cortex, 3) area TE1p on the lateral temporal
184 cortex, 4) area 7AL on the lateral parietal cortex, 5) area POS2 on the medial parietal cortex,
185 6) area 9-46d on the lateral prefrontal cortex, and 7) area 9m on the medial prefrontal cortex.

186 For each ROI, a streamline count map was generated by projecting the ROI-connected
187 callosal streamlines onto the mCC for each individual. The resultant maps were further
188 binarized and averaged across individuals, resulting a group pattern map (Fig. 2A).

189 For each cortical ROI above, we further evaluated the distribution of its callosal
190 connections on the contralateral hemisphere. The connection strength between this ROI
191 and HCPMMP regions on the contralateral hemisphere was measured by the fraction of
192 streamlines (FSe), which is calculated as the fraction of streamlines linking two regions
193 relative to the number of streamlines extrinsic to those regions (Donahue et al., 2016). The
194 FSe is conceptually analogous to the connection strength in retrograde-tracer-based studies
195 (Donahue et al., 2016), and has been increasingly used in recent studies (Zhao et al., 2019;
196 Hayashi et al., 2021; Rosen and Halgren, 2021). Likewise, the group FSe map was obtained
197 by averaging the FSe maps across individuals. For each ROI, the major connected
198 contralateral regions, i.e., accounting for at least 80% of total FSe value from this region,
199 were then extracted and displayed.

200 To assess how callosal streamline terminations in the contralateral hemisphere relate
201 to cortical gyral and sulcal features, we measured the proportion of streamlines that were
202 terminated on the cortical gyri.

203 For each mCC voxel, we also selected all passing callosal streamlines and calculated
204 the number of streamlines that were terminated in each HCPMMP cortical regions in the
205 left and right hemispheres, respectively. To quantify the similarity of the two hemispheric
206 streamline number patterns, we computed two measures: Pearson correlation (r) and
207 intraclass correlation coefficient (ICC), resulting an r map and an ICC map of mCC for
208 each individual as well as group-averaged r and ICC maps of mCC.

209 Finally, while neither tractography-based structural connectivity (SC) nor fMRI-based
210 functional connectivity (FC) is perfect, FC is more likely to reflect interhemispheric
211 connectivity between homotopic regions in the two hemispheres. We therefore evaluated
212 whether interhemispheric homotopic SC correlates with corresponding FC. To quantify the
213 SC for each HCPMMP homotopic regional pair, we used the FSe as above. The group-
214 averaged FSe was then generated and further log-transformed (Rosen and Halgren, 2021).
215 Regarding the FC estimation, the two HCP rs-fMRI sessions were used: REST1(919
216 subjects; female/male: 495/424) and REST2 (894 subjects; female/male: 482/412).
217 Specifically, we adopted the HCP minimally preprocessed rs-fMRI data, and the
218 preprocessing procedures included magnetic gradient distortion correction, EPI distortion
219 correction, nonbrain tissue removal, MNI standard space registration, and intensity
220 normalization (Glasser et al., 2013). The resultant data were then denoised by using
221 independent component analysis with the FIX tool (Salimi-Khorshidi et al., 2014). The
222 procedures of linear detrending, global signal regression and temporal bandpass filtering
223 (0.01-0.1 Hz) were further applied (Lowe and Russell, 1999; Cordes et al., 2001). For each
224 HCPMMP region, the averaged rs-fMRI time series across all vertices was calculated as
225 the regional rs-fMRI time series. For each HCPMMP homotopic regional pair, the FC
226 strength was measured using the Pearson correlation coefficient (converted to Fisher's Z-
227 values) between the two regional time series. The group-averaged FC was then generated
228 for each HCPMMP homotopic regional pair.

229 **WM microstructural measures on the mCC**

230 To measure callosal fiber composition, two widely used dMRI-derived parameters,
231 i.e., neurite density index (NDI) and fractional anisotropy (FA), were estimated for each

232 mCC voxel (Basser et al., 1994; Zhang et al., 2012). The mCC maps of NDI and FA were
233 further transformed to the standard mCC template space for each individual. The
234 representative NDI and FA maps in healthy adults were then generated by averaging all
235 HCP individual maps of the template space. Such representative maps were used to assess
236 the relevance of length scaling to callosal fiber composition.

237 **Mapping cortical topography of each mCC voxel**

238 For each HCP subject, the minimal preprocessing pipeline outputted FreeSurfer-
239 generated pial and white surfaces resampled onto the standard 32k_fs_LR mesh in the
240 native volume space. Each mCC voxel's streamlines were assigned to their closest vertex
241 on the white surface within a sphere with a 2-mm radius centered at its endpoint, therefore
242 yielding a standard 32K surface map of streamline counts for this voxel. For each voxel on
243 the mCC template, such a streamline count map on the standard 32K surface was
244 comparable across individuals. The group streamline count surface map was then obtained
245 by averaging the individual streamline count surface maps across all HCP individuals. We
246 applied a threshold to the group streamline count surface map to extract a binary cortical
247 topography map for each mCC voxel. Specifically, the mean + 0.5*standard deviation
248 (STD) of the group streamline count value across the entire surface was used as the main
249 threshold. To evaluate the influence of such a threshold on the results, we reran relevant
250 analyses by applying the following two thresholds: 1) a less stringent threshold, i.e., the
251 mean of the group streamline count value across the entire surface, and 2) a more stringent
252 threshold, i.e., the mean + 1*STD of the group streamline count value across the entire
253 surface.

254 **Cortical measures**

255 To assess the relevance of callosal fibers' length scaling to particular functional and
256 structural aspects of their connected cortical regions, we derived several cortical measures;
257 these measures are described below.

258 Functional lateralization index: We followed a recent study's methods to estimate the
259 cortical overall functional LI across cognitive domains (Karolis et al., 2019). First, we
260 selected available cognitive terms (575 in total) in the current Neurosynth database
261 (Yarkoni et al., 2011) (http://Neurosynth.org). We applied the Neurosynth tool for each
262 cognitive term to generate a whole-brain meta-activation image in MNI space. After
263 aligning this meta-activation image to a symmetric image template, we projected the values
264 onto the standard 32k_fs_LR mesh in MNI space. For each surface vertex, the absolute
265 between-hemisphere difference of the meta-activation values was calculated as the absolute
266 degree of functional lateralization for this cognitive term. To yield an overall functional LI
267 across all cognitive domains, we simply averaged the individual surface maps of functional
268 lateralization across all 575 cognitive terms.

269 Myelin content index: The group-averaged cortical T1w/T2w ratio-based myelin
270 content map, which was corrected for the transmit field bias, was estimated by Glasser and
271 colleagues (Glasser et al., 2021). We obtained this map from
272 *https://balsa.wustl.edu/file/show/zpL2m*, which is already on the standard 32k_fs_LR
273 surface mesh.

274 Evolutionary expansion index: The cortical expansion map in humans relative to
275 macaques was estimated by Hill and colleagues (Hill et al., 2010). We adopted the
276 expansion index and resampled the values onto the standard 32k_fs_LR surface mesh.

277 Human developmental expansion index: The cortical expansion map in human adults
278 relative to human infants was estimated by Hill and colleagues (Hill et al., 2010). Likewise,
279 we adopted the expansion index and resampled the values onto the standard 32k_fs_LR
280 surface mesh.

281 For each mCC voxel, we assigned the mean value of the aforementioned cortical
282 measure within its connected cortical region, resulting in one mCC map for the cortical
283 functional lateralization, cortical myelin content, evolutionary and developmental
284 expansion.

285 **Statistical analysis**

286 To determine whether the length scaling coefficient was related to callosal
287 microstructural measures and cortical measures above, we calculated the Spearman
288 correlations across all mCC voxels. We used the Spearman correlation because the length
289 scaling coefficient showed a nonnormal distribution on the mCC. A permutation test
290 (10,000 permutations) was adopted to estimate the Spearman correlation coefficient's
291 statistical significance (r_s). To evaluate the robustness and reproducibility of the observed
292 correlation across the analysis resolution of the mCC, we additionally parcellated the entire
293 mCC into ten segments. The parcellation scheme followed an influential mCC study, which
294 measured histological fiber density for each of the ten segments (Aboitiz et al., 1992).
295 Likewise, we assigned the mean callosal microstructural measures or the mean cortical
296 index value of the connected cortical region to each mCC segment. We then reran the
297 Spearman correlation analysis across all ten mCC segments.

298 To examine an independent relationship between callosal fiber length scaling and the
299 aforementioned cortical measures, we reran the Spearman correlations across the mCC
300 voxels or segments described above while controlling for the NDI and FA.
301

302 # Results

303 ## Validation of callosal tractography

304 As shown in Fig. 2, the streamlines from the primary motor cortex mainly traversed
305 the posterior body; the streamlines from the somatosensory cortex mainly traversed the
306 posterior body and anterior splenium; the streamlines from the lateral temporal cortex and
307 medial parietal cortex were tightly distributed on the posterior splenium; the streamlines
308 from the lateral parietal cortex were distributed on the anterior splenium. In contrast, the
309 streamlines from the lateral and medial prefrontal cortex were mostly clustered on the genu.
310 The observed spatial pattern on the mCC was strikingly similar for homotopic ROI pairs
311 on the left (Fig. 2) and right (Fig. S1) hemispheres, indicating the robustness of the result.
312 Importantly, these location patterns on the mCC are quite consistent with previous chemical
313 tracing findings in monkey and histological observations in human (Barbas and Pandya,
314 1984; de Lacoste et al., 1985; Rockland and Pandya, 1986; Caminiti et al., 2009, 2013;
315 Tomasi et al., 2012), therefore supporting the validity of our current CC tractography.

316 Fig. 3 illustrated the major callosal connections to regions on the contralateral
317 hemisphere (i.e., accounting for at least 80% of total FSe value) for the selected cortical
318 ROIs on the left hemisphere. As shown, the maximal FSe of the selected ROI was largely
319 located in the homotopic contralateral region, and major connections to the contralateral
320 hemisphere were concentrated around the homotopic and nearby regions. The only
321 exception was the cortical ROI on the lateral temporal cortex, which likely relates to
322 systematic biases of our current callosal tractography from the temporal lobe. The major
323 callosal connections to the contralateral hemisphere for the selected cortical ROIs on the
324 right hemisphere were illustrated in Fig. S2.

In line with previous anatomical observation (Xu et al., 2010; Nie et al., 2012; Budde and Annese, 2013; Chen et al., 2013), more gyrally terminated streamlines than sulcally terminated streamlines were observed in the vast majority of individuals (Fig. S3 and Fig. S4).

For all mCC voxels, their passing streamlines termination pattern on the hemisphere was quite similar between the two hemispheres (Fig. S5). This corresponds well with the largely mirrored nature of callosal connectional termination on the two hemispheres, therefore favoring the validity of our CC tractography.

However, we did not observe significant SC-FC correlation across the homotopic HCPMMP regional pairs (Fig. S6), which is consistent with a recent study (Rosen and Halgren, 2021). This negative result might reflect biases of our callosal tractography or biologically meaningful divergence between these two types of interhemispheric connectivity.

Callosal fiber variation in length scaling with brain size

As shown in Fig. 1, the measure of voxel-wise callosal fiber length on the mCC showed excellent test-retest reproducibility (ICC: 0.83 ± 0.18). The callosal fiber length scaling coefficients showed substantial variation across mCC voxels. Specifically, the rostrum, genu, anterior body, and posterior splenium showed the largest scaling coefficients, whereas the smallest values were in the posterior body and isthmus parts of the CC. The mCC scaling coefficient maps estimated from both the HCP and UKB datasets were strikingly similar (Spearman correlation $r_s = 0.91$, $p < 10^{-4}$), indicating excellent reproducibility for such a scaling pattern across the mCC. We further re-evaluated the length scaling map by defining the voxel-wise fiber length as the median and mode value

348 of all passing streamlines or by using the HCP unrelated samples to fit the log-log
349 regression model. The resulting patterns remain highly similar (data not shown), indicating
350 that the currently observed length scaling pattern on the mCC was also quite robust to the
351 computing methods for voxel-wise fiber length and the selected samples for regression
352 model fitting.

353 **Relevance to callosal fiber composition**

354 To determine whether the length scaling relates to underlying fiber composition, we
355 evaluated the Spearman correlation of the scaling coefficient with two popular dMRI-
356 derived WM microstructural parameters on the mCC: NDI and FA. Across all mCC voxels,
357 the length scaling coefficients were found to be positively correlated with NDI (HCP: r_s =
358 0.43, $p < 10^{-4}$; UKB: $r_s = 0.37$, $p < 10^{-4}$; Fig. 4A) and negatively correlated with FA (HCP:
359 $r_s = -0.05$, $p = 0.03$; UKB: $r_s = -0.12$, $p < 10^{-4}$; Fig. 4B). Moreover, we parcellated the mCC
360 into Aboitiz's ten segments, which measured histological fiber density for each of the ten
361 segments (Aboitiz et al., 1992). Across the ten mCC segments, significant correlation was
362 found between the histological fiber density of callosal fiber > 0.4μm and NDI ($r_s = 0.74$,
363 $p = 0.008$) but not with FA ($r_s = 0.12$, $p = 0.36$). There was no significant correlation
364 between the length scaling coefficient and NDI or FA (Fig. 4), possibly due to the limited
365 statistical power.

366 **Relevance to cortical functional lateralization**

367 The length scaling variation between callosal fibers putatively reflected cortical
368 differences in evolutionary or developmental demands for rapid interhemispheric
369 communication, which may have accounted for cortical differences in functional
370 lateralization of the human brain. To assess this hypothesis, we estimated an overall

371 functional lateralization index (LI) across cognitive domains (all 575 cognitive terms in the
372 current Neurosynth database) on the cortical surface (Fig. 5A) using a Neurosynth-based
373 meta-analysis (Yarkoni et al., 2011) (http://Neurosynth.org).

374 For each mCC voxel, we mapped its connected cortical region and calculated its
375 regional mean functional LI. Across all mCC voxels, the length scaling coefficients were
376 positively correlated with the functional LI (HCP: $r_s = 0.35$, $p < 10^{-4}$; UKB: $r_s = 0.30$, $p <$
377 10^{-4}; Fig. 5A). We also observed a positive correlation between length scaling and the
378 functional LI across the ten Aboitiz's segments (HCP: $r_s = 0.76$, $p = 0.006$; UKB: $r_s = 0.70$,
379 $p = 0.02$), indicating the robustness of this correlation. Therefore, stronger cortical
380 functional lateralization was accompanied by greater length scaling of the connected
381 callosal fibers, thus suggesting less demand for rapid cortical interhemispheric
382 communication. At both the voxel and segment levels, the partial Spearman correlations
383 after controlling for the NDI and FA remained significant, indicating an independent
384 relationship between callosal fiber length scaling and functional lateralization (Table 1).

385 **Relevance to cortical myelin content**

386 As illustrated in Fig. 5B, the length scaling coefficients were found to be negatively
387 correlated with cortical myelin content (across voxels: HCP, $r_s = -0.59$, $p < 10^{-4}$; UKB, $r_s =$
388 -0.59, $p < 10^{-4}$; across segments: HCP, $r_s = -0.76$, $p = 0.007$; UKB, $r_s = -0.71$, $p = 0.01$),
389 suggesting a biological link between cortical myeloarchitecture and interhemispheric
390 communication. After controlling for the NDI and FA, the partial Spearman correlations
391 remained significant at both voxel and segment level (Table 1).

392 **Relevance to cortical expansion**

393 To directly assess its evolutionary and developmental relevance, we investigated
394 whether the length scaling of callosal fibers was related to the evolutionary and
395 developmental expansion of their connected cortical regions, i.e., i) cortical expansion in
396 humans relative to macaques and ii) cortical expansion in human adults relative to human
397 infants. As described above, we assigned the mean cortical expansion index from the
398 connected cortical region to each mCC voxel/segment. As shown in Fig. 5C-D, the mCC
399 patterns of callosal fiber length scaling aligned well with those for the cortical expansion
400 index during evolution (across voxels: HCP, $r_s = 0.75$, $p < 10^{-4}$; UKB, $r_s = 0.55$, $p < 10^{-4}$;
401 across segments: HCP, $r_s = 0.75$, $p = 0.008$; UKB, $r_s = 0.76$, $p = 0.006$) and during
402 development (across voxels: HCP, $r_s = 0.48$, $p < 10^{-4}$; UKB, $r_s = 0.42$, $p < 10^{-4}$; across
403 segments: HCP, $r_s = 0.67$, $p = 0.02$; UKB, $r_s = 0.67$, $p = 0.02$). After controlling for the NDI
404 and FA, the partial Spearman correlations remained significant at both voxel and segment
405 level (Table 1).

406 **Callosal fibers of length over-scaling or under-scaling with brain size**

407 Theoretically, a callosal fiber length coefficient of 1/3 indicates iso-scaling with brain
408 size. In contrast, coefficients > 1/3 indicate that callosal fiber length scales more with
409 greater brain size (i.e., over-scaling), and coefficients < 1/3 indicate that callosal fiber
410 length scales less with brain size (i.e., under-scaling). As illustrated in Fig. 6A, significant
411 mCC clusters (false discovery rate, FDR corrected $p < 0.05$) existed for both over-scaling
412 and under-scaling. The overlapping regions between the clusters from the two datasets
413 were designated as the final clusters; one large cluster exhibited over-scaling, and two small
414 clusters demonstrated under-scaling (Fig. 6B). The over-scaling cluster covered most of

415 the anterior half of the mCC, which mainly connects the prefrontal cortices between the
416 two hemispheres. In contrast, the first under-scaling cluster was located on the splenium,
417 mainly connecting the precuneus and superior parietal lobule; the other under-scaling
418 cluster was on the posterior body, mainly connecting the paracentral lobule and precentral
419 gyrus (Fig. 6C).

420 As shown in Fig. 6E, the callosal fibers of over-scaling showed greater NDI value
421 ($t(826) = 15.1$, $p < 10^{-4}$) and smaller FA value ($t(826) = -10.9$, $p < 10^{-4}$), as well as stronger
422 functional lateralization ($t(8691) = 31.0$, $p < 10^{-4}$), less myelin content ($t(8691) = -67.6$, p
423 $< 10^{-4}$), and larger evolutionary and developmental expansion ($t(8691) = 67.6$, $p < 10^{-4}$;
424 $t(8691) = 42.2$, $p < 10^{-4}$) in their connected cortical regions, compared with the callosal
425 fibers of under-scaling. These results are compatible with the observed correlations of
426 callosal fiber scaling with respect to the fiber composition and cortical measures described
427 above.

428 Finally, our validation analyses confirmed the minimal influence of the procedure of
429 mapping the cortical topography of mCC voxels or segments on our results presented above
430 (Table 1 and Fig. 7).

431

Discussion

Our present study revealed substantial variation in length scaling with brain size among callosal fibers, ranging from under-scaling to iso- scaling to over-scaling, replicated in two large healthy cohorts. Fiber length under-scaling was mainly observed in callosal fibers connecting the precentral gyrus and parietal cortices, whereas over-scaling mainly involved callosal fibers connecting the prefrontal cortices. Notably, the variation in such length scaling was biologically meaningful: the length scaling of callosal fibers significantly correlated with underlying fiber composition, as well as with human functional lateralization, myelin content, evolutionary and developmental expansion of the fiber-connected cortical regions. Validation analyses confirmed excellent reproducibility and robustness of these observations.

Nonuniform length scaling of callosal fibers

The scaling patterns of GM features and midsagittal callosal size with brain size have been repeatedly studied, either across species or across human individuals (Jäncke et al., 1997; Rilling and Insel, 1999; Im et al., 2008; Herculano-Houzel, 2012; Mota and Herculano-Houzel, 2015; Reardon et al., 2018). In contrast, very few studies have been devoted to the scaling of WM fiber length with brain size, possibly due to technical difficulties in directly measuring fiber length *in vivo*. Our currently observed length scaling of callosal fibers and its biological relevance proved the overall feasibility and importance of studying WM fibers' length scaling.

Notably, our current fiber length was estimated from dMRI tractography, so far the only technique of reconstructing WM fiber *in-vivo.* This widely-used technique however is inherently limited, showing errors and biases in resultant fiber streamlines particularly

455 for long range WM tracts (Reveley et al., 2015; Donahue et al., 2016). To minimize these
456 errors, the present study adopted high-angular resolution dMRI data, cutting-edge local
457 orientation modeling, and tractography algorithm, i.e., the requirements for the most
458 reliable fiber tracking. Moreover, we performed extensive validation analyses on our
459 callosal tractography. While most validation results provided support for the overall
460 validity of our callosal tractography, a few validation results suggested the existence of
461 tractography biases. For example, the observed dispersion of callosal connected
462 contralateral regions from the lateral temporal cortex (Fig. 3) likely reflects a systematic
463 tendency or bias of callosal streamlines to avoid trajectories to the temporal lobe. In
464 addition, the validity of our callosal tractography could be challenged to some extent by
465 the lack of correlation between interhemispheric structural connectivity and functional
466 connectivity (Fig. S6). Given these methodological limitations, the observed variation of
467 length scaling among callosal fibers should be interpreted cautiously.

468 The substantial variation in length scaling suggests a change in the relative length
469 among callosal fibers in larger brains. Such length reorganization in larger brains is
470 unlikely confined to the CC but extrapolates to other WM fibers across the entire brain. On
471 the other hand, previous studies have demonstrated fiber diameter/myelination
472 reorganization in larger brains (Wang et al., 2008; Phillips et al., 2015). Thus, larger brains
473 choose to jointly adjust the two critical determinants of conduction delay, i.e., fiber
474 diameter/myelination and length, to reach an optimal fiber composition of the entire brain
475 to achieve structural and functional efficacy best. Such a strategy is theoretically
476 advantageous compared to solely adjusting either fiber diameter/myelination or length. The
477 joint adjustment strategy offers a larger search space for the optimal fiber reorganization

478 solution by providing two-parameter dimensions. Notably, the median or mean diameter
479 of callosal fibers did not significantly differ between species or human individuals,
480 although the largest diameter of callosal fibers did increase in species with larger brains
481 (Olivares et al., 2001; Wang et al., 2008). Therefore, larger brains seem to adjust the
482 relative length across the CC more than they adjust the fiber diameter/myelination. This
483 particular adjustment model might be specific to the CC, and its underlying mechanisms
484 deserve further investigation.

485 Callosal fiber density and diameters also exhibited significant variation in the mCC,
486 as revealed by human histology (Aboitiz et al., 1992). Callosal fibers with larger diameters
487 mainly connect sensorimotor cortices, and small diameters connect association cortices
488 (Caminiti et al., 2013). This particular pattern reflects functional differences in cross-
489 hemisphere communication among different types of cortical areas; sensorimotor functions
490 require rapid interhemispheric information integration, and higher cognitive functions in
491 association cortices work well with slow interhemispheric information transfer. In the
492 present study, one of our observed under-scaling clusters was around the mCC posterior
493 body, mainly connecting the sensorimotor cortex; the only cluster of over-scaling
494 predominantly connected the prefrontal lobe—the primary association cortex. Therefore,
495 the requirement of rapid communication between bilateral sensorimotor areas is
496 accomplished by both larger fiber diameter and under-increased fiber length in larger brains.
497 Smaller fiber diameter and an overly increased fiber length contribute to slower
498 interhemispheric communication between bilateral association cortices. The rapid
499 interhemispheric communication for low-level cortices but the slow interhemispheric

500 communication for high-level cortices may reflect a general principle of the functional
501 organization across species and individuals.

502 **Biological relevance of callosal fiber length scaling**

503 The present study used two dMRI parameters to estimate the spatial pattern of mCC
504 fiber composition *in-vivo*. Notably, in contrast to the FA, the NDI showed a strong
505 correlation with the influential Aboitiz's histological fiber density, so far the golden
506 standard for such a measure (Aboitiz et al., 1992). This strongly verifies that the NDI can
507 sensitively reflect axonal density in uncrossing areas (e.g., mCC), supporting relevant
508 applications for this particular imaging parameter. Putatively, lower fiber density comes
509 with a larger local fiber diameter on the mCC. The mCC FA did not correlate with
510 histological fiber density and may reflect the myelination degree (Chang et al., 2017). The
511 observed length scaling's positive correlation with NDI and negative correlation with FA
512 suggested that callosal fibers of less length scaling (i.e., smaller increase in fiber length)
513 had lower density, larger diameter, and were myelinated. These empirical pieces of
514 evidence support that smaller increase in fiber length, larger fiber diameter, and increased
515 myelination are simultaneously implemented to jointly facilitate rapid interhemispheric
516 communications of particular cortical regions in larger brains. On the other hand, the
517 association between these callosal fiber characteristics may relate to cost control of fiber
518 reorganization in larger brains: to save physical space and energy consumption, highly
519 myelinated callosal fibers of large diameter tend to minimize their length increase as
520 possible. Future studies are encouraged to relate the length scaling with other nontrivial
521 callosal measures, e.g., midsagittal callosal thickness (Park et al., 2011).

522 Interhemispheric communication efficacy has long been considered a contributing
523 factor to the emergence of functional lateralization. According to Ringo's influential
524 hypothesis, the excessive callosal conduction delay of larger brains leads to functional
525 lateralization (Ringo et al., 1994). In contrast, functional lateralization may arise due to
526 inter-hemispheric inhibition through callosal fibers (Cook, 1984). Measurements of the
527 mCC area or dMRI parameters have been repeatedly used as a proxy for callosal
528 connectivity to test these hypotheses (Bloom and Hynd, 2005; van der Knaap and van der
529 Ham, 2011), with contrasting results. Both positive and negative correlations between
530 callosal connectivity and functional lateralization have been reported (Josse et al., 2008;
531 Karolis et al., 2019), supporting both hypotheses. By directly measuring callosal length,
532 our observations suggested that more scaling of callosal fiber length (i.e., a relatively
533 greater conduction delay in larger brains) is accompanied by stronger functional
534 lateralization, therefore favoring Ringo's hypothesis but not the inhibition hypothesis.
535 Ringo's original hypothesis did specify that an excessive interhemispheric conduction
536 delay, which leads to functional lateralization, is mainly caused by increased callosal fiber
537 length due to brain size expansion. Our observed positive correlation of callosal length
538 scaling with functional lateralization provides more direct support for this influential
539 hypothesis.

540 The association of the callosal fiber length scaling with cortical expansion during
541 evolution and postnatal development provides direct support for evolutionary and
542 developmental contributions to scaling variation. For a cortical region, less demand for
543 rapid interhemispheric communication (as reflected by greater length scaling) and greater
544 expansion of the cortical area are likely rooted in the same motivations for the entire brain's

545 optimal functional efficiency. As revealed previously, expansion of the cortical area across
546 human individuals also showed under-scaling, iso-scaling, over-scaling with greater brain
547 size (Reardon et al., 2018). The under- and over-expansion of cortical regions with greater
548 brain size were attributed mainly to under- or over- increased cortical folding (Zilles et al.,
549 2013). Notably, cortical expansion can be achieved by modifying the degree of cortical
550 folding, surface outward degree, or both. Given the U shape of callosal fibers, their length
551 scaling can partly represent their connected cortical regions' outward surface degree.
552 Therefore, the observation of callosal fiber length under- or over-scaling provides evidence
553 for the contributing role of the surface outward degree in under- or over-expansion of the
554 cortical area across individuals or during evolution and development. However, for specific
555 regions, the extent that the changes in cortical folding degree or outward surface degree
556 contribute to the evolutionary and developmental expansion of the cortical area remains
557 elusive.

558 Nevertheless, biological mechanisms underlying the association of the length scaling
559 with the nontrivial callosal and cortical measures remain unclear. It might relate to the
560 shared genetic or environmental factors. At the neural level, causal relationships could exist
561 among these fiber and cortical characteristics. Animal studies are warranted in the future
562 in order to evaluate these speculations.

563 In conclusion, the current findings of callosal fiber variation in length scaling with
564 brain size provide direct empirical evidence for length reorganization among WM fibers in
565 larger brains. These observations also highlight the interactions of evolutionary and
566 developmental constraints with interhemispheric communication.

567

References

Aboitiz F, Scheibel AB, Fisher RS, Zaidel E (1992) Fiber composition of the human corpus callosum. Brain Res 598:143–153.

Alfaro-Almagro F et al. (2018) Image processing and Quality Control for the first 10,000 brain imaging datasets from UK Biobank. Neuroimage 166:400–424.

Barbas H, Pandya DN (1984) Topography of commissural fibers of the prefrontal cortex in the rhesus monkey. Exp Brain Res 55:187–191.

Basser PJ, Mattiello J, LeBihan D (1994) Estimation of the effective self-diffusion tensor from the NMR spin echo. J Magn Reson B 103:247–254.

Bloom JS, Hynd GW (2005) The role of the corpus callosum in interhemispheric transfer of information: excitation or inhibition? Neuropsychol Rev 15:59–71.

Budde M, Annese J (2013) Quantification of anisotropy and fiber orientation in human brain histological sections. Frontiers in Integrative Neuroscience 7:3.

Caminiti R, Carducci F, Piervincenzi C, Battaglia-Mayer A, Confalone G, Visco-Comandini F, Pantano P, Innocenti GM (2013) Diameter, length, speed, and conduction delay of callosal axons in macaque monkeys and humans: comparing data from histology and magnetic resonance imaging diffusion tractography. J Neurosci 33:14501–14511.

Caminiti R, Ghaziri H, Galuske R, Hof PR, Innocenti GM (2009) Evolution amplified processing with temporally dispersed slow neuronal connectivity in primates. Proc Natl Acad Sci U S A 106:19551–19556.

589 Chang EH, Argyelan M, Aggarwal M, Chandon T-SS, Karlsgodt KH, Mori S, Malhotra
590 AK (2017) The role of myelination in measures of white matter integrity:
591 Combination of diffusion tensor imaging and two-photon microscopy of CLARITY
592 intact brains. Neuroimage 147:253–261.

593 Chen H, Zhang T, Guo L, Li K, Yu X, Li L, Hu X, Han J, Hu X, Liu T (2013)
594 Coevolution of Gyral Folding and Structural Connection Patterns in Primate Brains.
595 Cereb Cortex 23:1208–1217.

596 Cook ND (1984) Homotopic callosal inhibition. Brain and Language 23:116–125.

597 Cordes D, Haughton VM, Arfanakis K, Carew JD, Turski PA, Moritz CH, Quigley MA,
598 Meyerand ME (2001) Frequencies Contributing to Functional Connectivity in the
599 Cerebral Cortex in "Resting-state" Data. AJNR Am J Neuroradiol 22:1326–1333.

600 de Lacoste MC, Kirkpatrick JB, Ross ED (1985) Topography of the human corpus
601 callosum. J Neuropathol Exp Neurol 44:578–591.

602 Donahue CJ, Sotiropoulos SN, Jbabdi S, Hernandez-Fernandez M, Behrens TE, Dyrby
603 TB, Coalson T, Kennedy H, Knoblauch K, Van Essen DC, Glasser MF (2016) Using
604 Diffusion Tractography to Predict Cortical Connection Strength and Distance: A
605 Quantitative Comparison with Tracers in the Monkey. J Neurosci 36:6758–6770.

606 Genovese CR, Lazar NA, Nichols T (2002) Thresholding of statistical maps in functional
607 neuroimaging using the false discovery rate. Neuroimage 15:870–878.

608 Glasser MF, Coalson TS, Harms MP, Baum GL, Autio JA, Auerbach EJ, Xu J, Greve
609 DN, Yacoub E, Van Essen DC, Bock NA, Hayashi T (2021) Transmit Field Bias
610 Correction of T1w/T2w Myelin Maps. bioRxiv:2021.08.08.455570.

611 Glasser MF, Coalson TS, Robinson EC, Hacker CD, Harwell J, Yacoub E, Ugurbil K,
612 Andersson J, Beckmann CF, Jenkinson M, Smith SM, Van Essen DC (2016) A
613 multi-modal parcellation of human cerebral cortex. Nature 536:171–178.

614 Glasser MF, Sotiropoulos SN, Wilson JA, Coalson TS, Fischl B, Andersson JL, Xu J,
615 Jbabdi S, Webster M, Polimeni JR, Van Essen DC, Jenkinson M (2013) The
616 minimal preprocessing pipelines for the Human Connectome Project. Neuroimage
617 80:105–124.

618 Hayashi T, Hou Y, Glasser MF, Autio JA, Knoblauch K, Inoue-Murayama M, Coalson T,
619 Yacoub E, Smith S, Kennedy H, Van Essen DC (2021) The nonhuman primate
620 neuroimaging and neuroanatomy project. NeuroImage 229:117726.

621 Herculano-Houzel S (2012) The remarkable, yet not extraordinary, human brain as a
622 scaled-up primate brain and its associated cost. Proc Natl Acad Sci U S A 109 Suppl
623 1:10661–10668.

624 Herculano-Houzel S, Mota B, Wong P, Kaas JH (2010) Connectivity-driven white matter
625 scaling and folding in primate cerebral cortex. Proc Natl Acad Sci U S A
626 107:19008–19013.

627 Hill J, Inder T, Neil J, Dierker D, Harwell J, Van Essen D (2010) Similar patterns of
628 cortical expansion during human development and evolution. Proc Natl Acad Sci U
629 S A 107:13135–13140.

630 Im K, Lee J-M, Lyttelton O, Kim SH, Evans AC, Kim SI (2008) Brain size and cortical
631 structure in the adult human brain. Cereb Cortex 18:2181–2191.

632 Jäncke L, Staiger JF, Schlaug G, Huang Y, Steinmetz H (1997) The relationship between
633 corpus callosum size and forebrain volume. Cerebral Cortex 7:48–56.

634 Jeurissen B, Tournier J-D, Dhollander T, Connelly A, Sijbers J (2014) Multi-tissue
635 constrained spherical deconvolution for improved analysis of multi-shell diffusion
636 MRI data. Neuroimage 103:411–426.

637 Josse G, Seghier ML, Kherif F, Price CJ (2008) Explaining function with anatomy:
638 language lateralization and corpus callosum size. J Neurosci 28:14132–14139.

639 Kaas JH (2000) Why is Brain Size so Important: Design Problems and Solutions as
640 Neocortex Gets Biggeror Smaller. Brain and Mind 1:7–23.

641 Karolis VR, Corbetta M, Thiebaut de Schotten M (2019) The architecture of functional
642 lateralisation and its relationship to callosal connectivity in the human brain. Nat
643 Commun 10:1417.

644 Lowe MJ, Russell DP (1999) Treatment of baseline drifts in fMRI time series analysis. J
645 Comput Assist Tomogr 23:463–473.

646 Miller KL et al. (2016) Multimodal population brain imaging in the UK Biobank
647 prospective epidemiological study. Nature neuroscience 19:1523–1536.

648 Mota B, Herculano-Houzel S (2015) BRAIN STRUCTURE. Cortical folding scales
649 universally with surface area and thickness, not number of neurons. Science 349:74–
650 77.

651 Nie J et al. (2012) Axonal fiber terminations concentrate on gyri. Cereb Cortex 22:2831–
652 2839.

653 Olivares R, Montiel J, Aboitiz F (2001) Species differences and similarities in the fine
654 structure of the mammalian corpus callosum. Brain Behav Evol 57:98–105.

655 Park J-S, Yoon U, Kwak K-C, Seo SW, Kim SI, Na DL, Lee J-M (2011) The
656 relationships between extent and microstructural properties of the midsagittal corpus
657 callosum in human brain. NeuroImage 56:174–184.

658 Phillips KA, Stimpson CD, Smaers JB, Raghanti MA, Jacobs B, Popratiloff A, Hof PR,
659 Sherwood CC (2015) The corpus callosum in primates: processing speed of axons
660 and the evolution of hemispheric asymmetry. Proc Biol Sci 282:20151535.

661 Reardon PK, Seidlitz J, Vandekar S, Liu S, Patel R, Park MTM, Alexander-Bloch A,
662 Clasen LS, Blumenthal JD, Lalonde FM, Giedd JN, Gur RC, Gur RE, Lerch JP,
663 Chakravarty MM, Satterthwaite TD, Shinohara RT, Raznahan A (2018) Normative
664 brain size variation and brain shape diversity in humans. Science 360:1222–1227.

665 Reveley C, Seth AK, Pierpaoli C, Silva AC, Yu D, Saunders RC, Leopold DA, Ye FQ
666 (2015) Superficial white matter fiber systems impede detection of long-range
667 cortical connections in diffusion MR tractography. Proc Natl Acad Sci U S A
668 112:E2820–E2828.

669 Rilling JK, Insel TR (1999) Differential expansion of neural projection systems in
670 primate brain evolution. Neuroreport 10:1453–1459.

671 Ringo JL, Doty RW, Demeter S, Simard PY (1994) Time is of the essence: a conjecture
672 that hemispheric specialization arises from interhemispheric conduction delay.
673 Cereb Cortex 4:331–343.

674 Rockland KS, Pandya DN (1986) Topography of occipital lobe commissural connections
675 in the rhesus monkey. Brain Res 365:174–178.

676 Rosen BQ, Halgren E (2021) A Whole-Cortex Probabilistic Diffusion Tractography
677 Connectome. eNeuro 8.

678 Salimi-Khorshidi G, Douaud G, Beckmann CF, Glasser MF, Griffanti L, Smith SM
679 (2014) Automatic denoising of functional MRI data: combining independent
680 component analysis and hierarchical fusion of classifiers. Neuroimage 90:449–468.

681 Smith RE, Tournier J-D, Calamante F, Connelly A (2012) Anatomically-constrained
682 tractography: improved diffusion MRI streamlines tractography through effective
683 use of anatomical information. Neuroimage 62:1924–1938.

684 Smith SM, Jenkinson M, Woolrich MW, Beckmann CF, Behrens TEJ, Johansen-Berg H,
685 Bannister PR, De Luca M, Drobnjak I, Flitney DE, Niazy RK, Saunders J, Vickers J,
686 Zhang Y, De Stefano N, Brady JM, Matthews PM (2004) Advances in functional
687 and structural MR image analysis and implementation as FSL. Neuroimage 23 Suppl
688 1:S208-219.

689 Thirion JP (1998) Image matching as a diffusion process: an analogy with Maxwell's
690 demons. Med Image Anal 2:243–260.

691 Tomasi S, Caminiti R, Innocenti GM (2012) Areal differences in diameter and length of
692 corticofugal projections. Cereb Cortex 22:1463–1472.

693 Tournier J-D, Calamante F, Connelly A (2007) Robust determination of the fibre
694 orientation distribution in diffusion MRI: non-negativity constrained super-resolved
695 spherical deconvolution. Neuroimage 35:1459–1472.

696 Tournier J-D, Smith R, Raffelt D, Tabbara R, Dhollander T, Pietsch M, Christiaens D,
697 Jeurissen B, Yeh C-H, Connelly A (2019) MRtrix3: A fast, flexible and open
698 software framework for medical image processing and visualisation. Neuroimage
699 202:116137.

700 van der Knaap LJ, van der Ham IJM (2011) How does the corpus callosum mediate
701 interhemispheric transfer? A review. Behav Brain Res 223:211–221.

702 Van Essen DC et al. (2012) The Human Connectome Project: a data acquisition
703 perspective. Neuroimage 62:2222–2231.

704 Van Essen DC (2018) Scaling of human brain size. Science 360:1184–1185.

705 Vercauteren T, Pennec X, Perchant A, Ayache N (2009) Diffeomorphic demons: efficient
706 non-parametric image registration. Neuroimage 45:S61-72.

707 Wang SS-H, Shultz JR, Burish MJ, Harrison KH, Hof PR, Towns LC, Wagers MW,
708 Wyatt KD (2008) Functional trade-offs in white matter axonal scaling. J Neurosci
709 28:4047–4056.

710 Waxman SG, Kocsis JD, Stys PK (1995) The axon: structure, function, and
711 pathophysiology. Oxford University Press, USA.

712 Xu G, Knutsen AK, Dikranian K, Kroenke CD, Bayly PV, Taber LA (2010) Axons pull
713 on the brain, but tension does not drive cortical folding. J Biomech Eng 132:071013.

714 Yarkoni T, Poldrack RA, Nichols TE, Van Essen DC, Wager TD (2011) Large-scale
715 automated synthesis of human functional neuroimaging data. Nature Methods
716 8:665–670.

Zhang H, Schneider T, Wheeler-Kingshott CA, Alexander DC (2012) NODDI: Practical in vivo neurite orientation dispersion and density imaging of the human brain. NeuroImage 61:1000–1016.

Zhang K, Sejnowski TJ (2000) A universal scaling law between gray matter and white matter of cerebral cortex. Proc Natl Acad Sci U S A 97:5621–5626.

Zhao C, Yang L, Xie S, Zhang Z, Pan H, Gong G (2019) Hemispheric Module-Specific Influence of the X Chromosome on White Matter Connectivity: Evidence from Girls with Turner Syndrome. Cerebral Cortex 29:4580–4594.

Zilles K, Palomero-Gallagher N, Amunts K (2013) Development of cortical folding during evolution and ontogeny. Trends Neurosci 36:275–284.

Table 1. The full and partial Spearman correlation of the callosal fiber length scaling with cortical measures under different cortical mapping thresholds.

			Cortical mapping threshold					
			Mean + 0.5*STD		Mean		Mean + 1*STD	
			HCP	UKB	HCP	UKB	HCP	UKB
Functional lateralization	**Voxel**	Full	0.35 ($p<10^{-4}$)***	0.30 ($p<10^{-4}$)***	0.34 ($p<10^{-4}$)***	0.30 ($p<10^{-4}$)***	0.32 ($p<10^{-4}$)***	0.27 ($p<10^{-4}$)***
		Partial	0.24 ($p<10^{-4}$)***	0.17 ($p<10^{-4}$)***	0.21 ($p<10^{-4}$)***	0.15 ($p<10^{-4}$)***	0.22 ($p<10^{-4}$)***	0.14 ($p<10^{-4}$)***
	Segment	Full	0.76 (p=0.006)**	0.70 (p=0.02)*	0.67 (p=0.02)*	0.60 (p=0.04)*	0.78 (p=0.004)**	0.75 (p=0.009)**
		Partial	0.71 (p=0.02)*	0.63 (p=0.03)*	0.61 (p=0.04)*	0.51 (p=0.08)	0.74 (p=0.01)*	0.68 (p=0.02)*
Myelin content	**Voxel**	Full	-0.59 ($p<10^{-4}$)***	-0.59 ($p<10^{-4}$)***	-0.64 ($p<10^{-4}$)***	-0.64 ($p<10^{-4}$)***	-0.53 ($p<10^{-4}$)***	-0.55 ($p<10^{-4}$)***
		Partial	-0.23 ($p<10^{-4}$)***	-0.21 ($p<10^{-4}$)***	-0.29 ($p<10^{-4}$)***	-0.26($p<10^{-4}$)***	-0.14($p<10^{-4}$)***	-0.16 ($p<10^{-4}$)***
	Segment	Full	-0.76 (p=0.007)**	-0.71 (p=0.01)*	-0.82 (p=0.002)**	-0.71 (p=0.01)*	-0.79 (p=0.003)**	-0.71 (p=0.01)*
		Partial	-0.70 (p=0.02)*	-0.61 (p=0.05)*	-0.78 (p=0.008)**	-0.61 (p=0.04)*	-0.75 (p=0.01)*	-0.62 (p=0.04)*
Evolutionary expansion	**Voxel**	Full	0.70 ($p<10^{-4}$)***	0.55 ($p<10^{-4}$)***	0.64 ($p<10^{-4}$)***	0.52 ($p<10^{-4}$)***	0.69 ($p<10^{-4}$)***	0.55 ($p<10^{-4}$)***
		Partial	0.64 ($p<10^{-4}$)***	0.37 ($p<10^{-4}$)***	0.53 ($p<10^{-4}$)***	0.32 ($p<10^{-4}$)***	0.64 ($p<10^{-4}$)***	0.37 ($p<10^{-4}$)***
	Segment	Full	0.75 (p=0.008)**	0.76 (p=0.006)**	0.65 (p=0.02)*	0.60 (p=0.04)*	0.75 (p=0.007)**	0.70 (p=0.01)*
		Partial	0.70 (p=0.02)*	0.67 (p=0.02)*	0.56 (p=0.06)	0.46 (p=0.1)	0.73 (p=0.01)*	0.58 (p=0.05)
Developmental expansion	**Voxel**	Full	0.48 ($p<10^{-4}$)***	0.42 ($p<10^{-4}$)***	0.34 ($p<10^{-4}$)***	0.27 ($p<10^{-4}$)***	0.52 ($p<10^{-4}$)***	0.45 ($p<10^{-4}$)***
		Partial	0.52 ($p<10^{-4}$)***	0.35 ($p<10^{-4}$)***	0.42 ($p<10^{-4}$)***	0.25 ($p<10^{-4}$)***	0.54 ($p<10^{-4}$)***	0.35 ($p<10^{-4}$)***
	Segment	Full	0.67 (p=0.02)*	0.67 (p=0.02)*	0.59 (p=0.04)*	0.54 (p=0.06)	0.67 (p=0.02)*	0.67 (p=0.02)*
		Partial	0.74 (p=0.01)*	0.60 (p=0.04)*	0.61 (p=0.04)*	0.29 (p=0.2)	0.74 (p=0.01)*	0.60 (p=0.04)*

*: p <0.05; **: p <0.01; and ***: p <0.001. The significant Spearman correlation coefficient ($\boldsymbol{r_s}$) are highlighted in gray. For the partial correlation, the neurite density index (NDI) and fractional anisotropy (FA) were included as covariates.

Figures

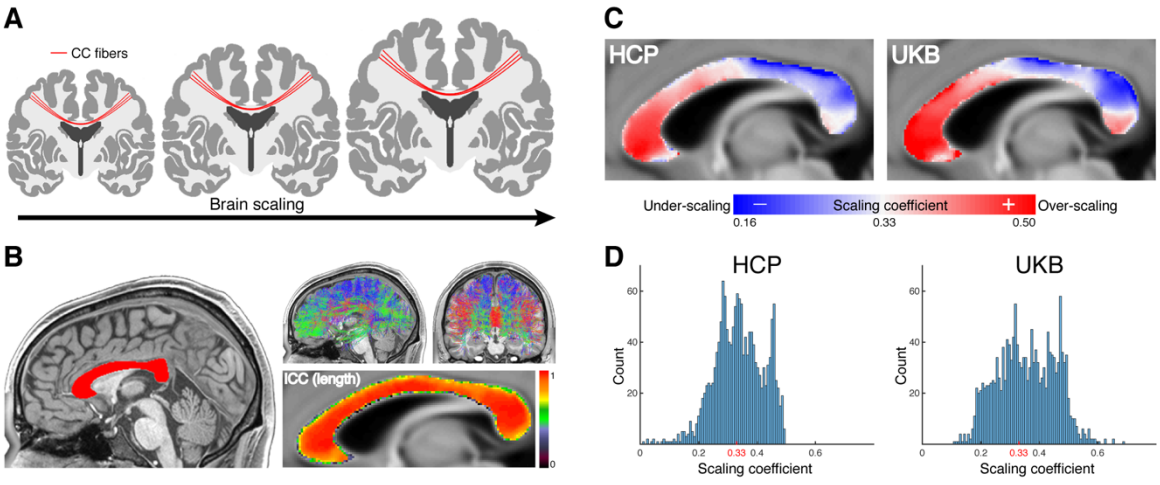

Fig. 1. Callosal fiber variation in length scaling with brain size. (A) Schematic of callosal fiber length scaling with brain size. (B) The midsagittal CC (red) and callosal fibers from one example subject. The fiber length measure showed high intraclass correlation coefficient (ICC) values, suggesting excellent test-retest reproducibility. (C) Callosal fiber length scaling coefficient maps of the HCP and UKB datasets. (D) The histogram of scaling coefficients. The iso-scaling coefficient 0.33 is highlighted in red.

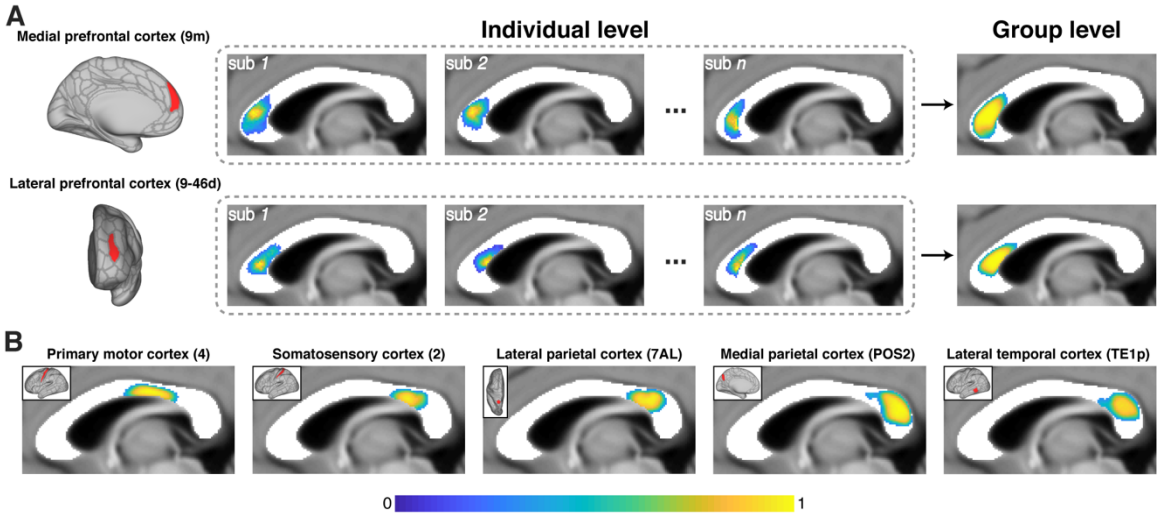

Fig. 2. Callosal streamlines' passing location on the mCC for selected cortical regions. (A) Schematic diagram of generating group mCC location for a cortical region. As illustrated, the passing location on the mCC can overlap to some degree for two different cortical regions (e.g., area 9-46d on the lateral prefrontal cortex and area 9m on the medial prefrontal cortex). (B) The resultant group mCC pattern maps are displayed for selected HCPMMP regions on the left hemisphere (red in the solid box): area 4 on the primary motor cortex, area 2 on the somatosensory cortex, area TE1p on the lateral temporal cortex, area 7AL on the lateral parietal cortex, and area POS2 on the medial parietal cortex. The HCPMMP regional abbreviation is included in the bracket.

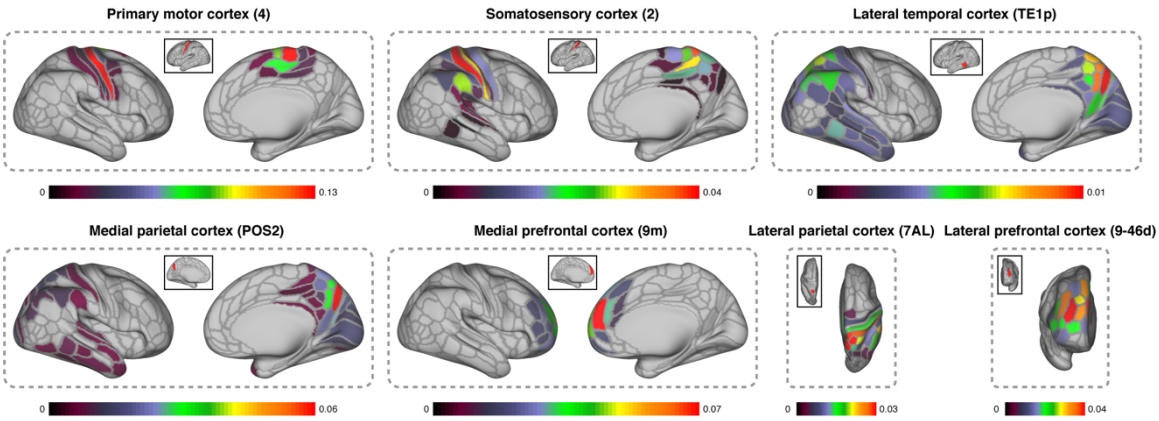

Fig. 3. Major callosal connections to the contralateral hemisphere for selected cortical regions. For each cortical region, the top strongly connected regions on the contralateral hemisphere are displayed, which together account for at least 80% of total fraction of streamline (FSe) value from this region. The group FSe maps are displayed for selected HCPMMP regions on the left hemisphere (red in the solid box): area 4 on the primary motor cortex, area 2 on the somatosensory cortex, area TE1p on the lateral temporal cortex, area 7AL on the lateral parietal cortex, area POS2 on the medial parietal cortex, area 9-46d on the lateral prefrontal cortex, and area 9m on the medial prefrontal cortex. The HCPMMP regional abbreviation is included in the bracket. The color bar indicates the FSe value from the selected cortical region.

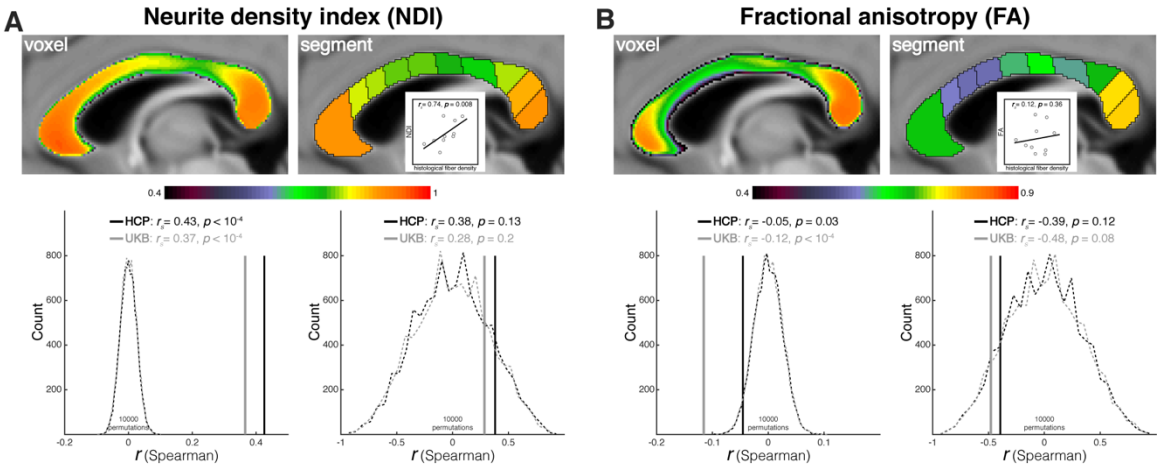

Fig. 4. Relevance to callosal fiber composition. The relationships between callosal fiber length scaling and neurite density index (A), and fractional anisotropy (B). Top row is the group-averaged neurite density index (NDI) and fractional anisotropy (FA) at the voxel and segment level. The scatter plots of NDI and FA against the Aboitiz's histological callosal fiber density are displayed at the segment level. Bottom row is the Spearman correlation between the microstructural measures and callosal fiber length scaling coefficient across midsagittal CC voxels and segments. Black: HCP, Gray: UKB. Solid lines represent empirical Spearman correlation coefficients; dashed lines represent the null distribution of Spearman correlation coefficients derived from 10,000 permutations.

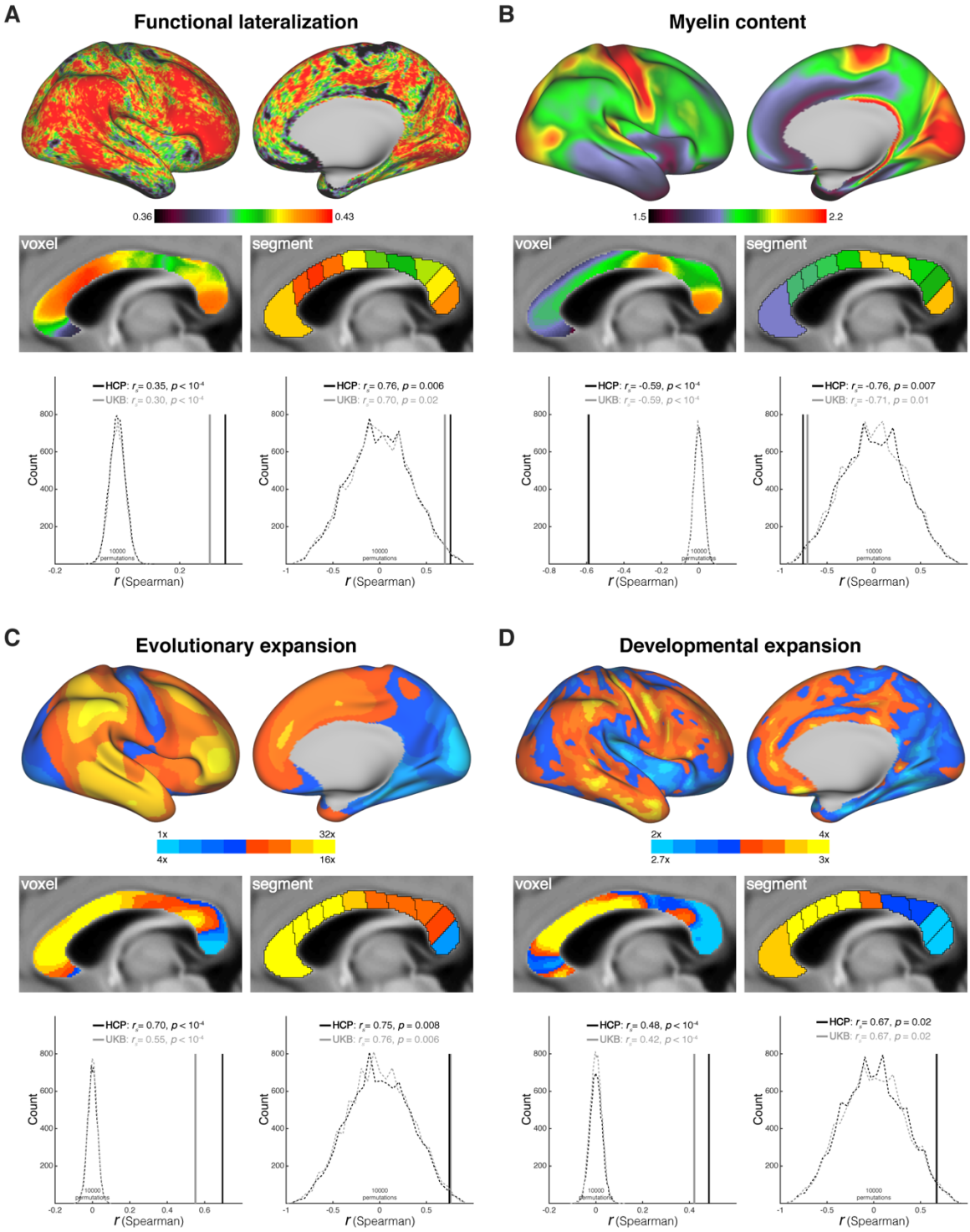

Fig. 5. Relevance to cortical measures. The relationships between callosal fiber length scaling and cortical functional lateralization (A), myelin content (B), evolutionary cortical expansion of the primate brain (C), and developmental cortical expansion of the human

brain (D). Top row is the averaged cortical functional lateralization map across cognitive terms, averaged myelin content map across HCP subjects, evolutionary cortical expansion map, and developmental cortical expansion map, respectively. Middle row is the cortical measures of the midsagittal CC at the voxel and segment level. Bottom row is the Spearman correlation between the cortical measures and callosal fiber length scaling coefficient across midsagittal CC voxels and segments. Black: HCP, Gray: UKB. Solid lines represent empirical Spearman correlation coefficients; dashed lines represent the null distribution of Spearman correlation coefficients derived from 10,000 permutations.

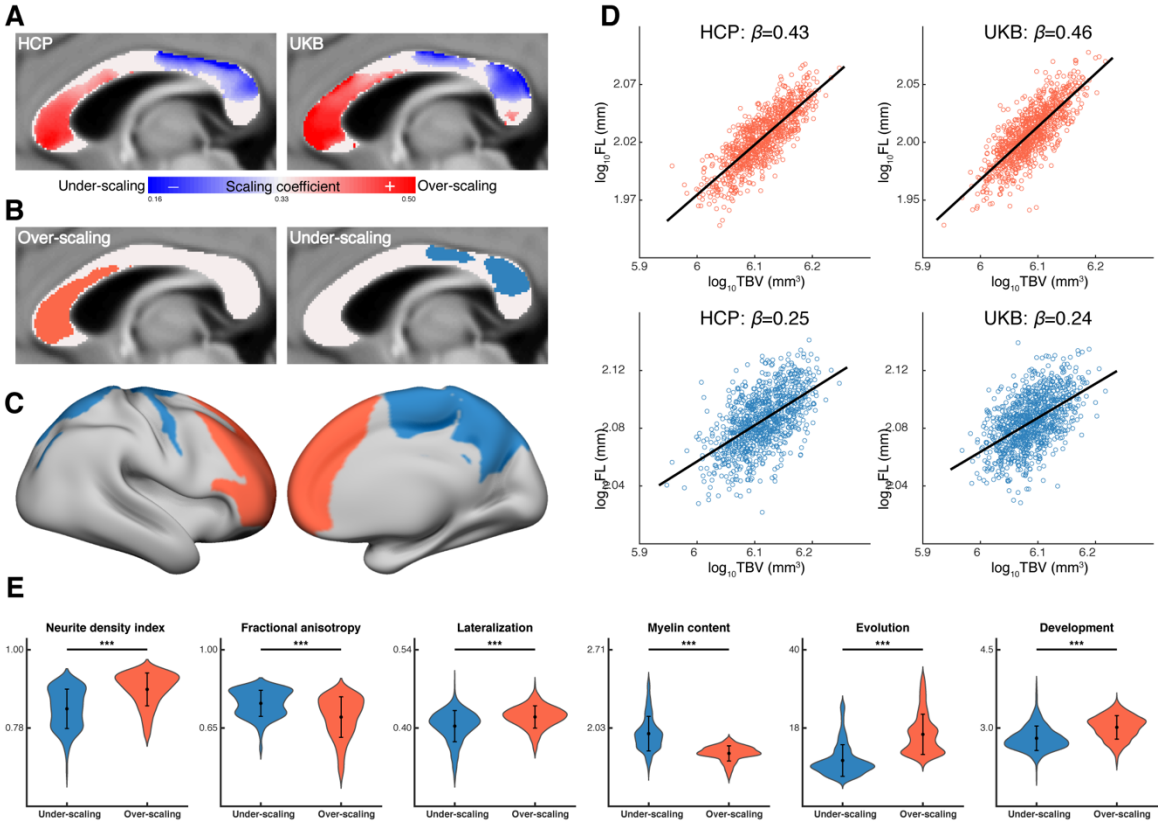

Fig. 6. Callosal fibers of length over-scaling or under-scaling with brain size. (A) The midsagittal CC areas showing significant fiber length over-scaling or under-scaling. (B) The conjunction midsagittal CC area of length over-scaling or under-scaling between the HCP and UKB datasets. Left panel: over-scaling clusters. Right panel: under-scaling clusters. (C) The cortical regions connected by the callosal fibers passing through the over-scaling and under-scaling clusters. (D) Scatter plots of the logarithm of fiber length and the logarithm of TBV for the over-scaling (i.e., significant beta > 0.33) and under-scaling (i.e., significant beta < 0.33) clusters. (E) The differences between the over-scaling and under-scaling clusters in the two white matter microstructural measures and four cortical measures above. The mean (black dot) and standard deviation are overlaid on the violin map. ***: $p < 0.001$. Orange: over-scaling clusters. Blue: under-scaling clusters.

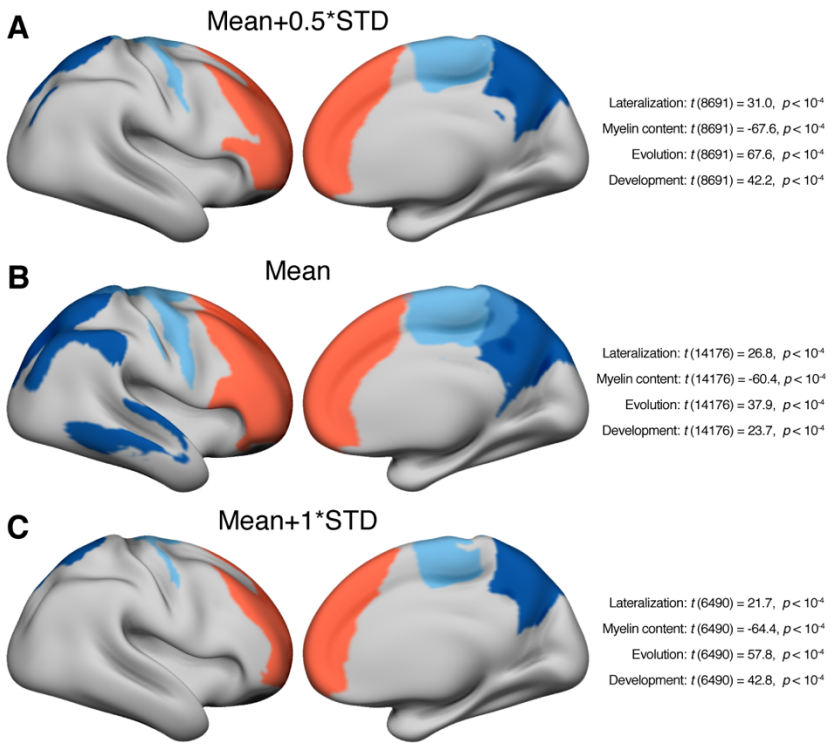

Fig. 7. Cortical topography of the mCC clusters showing fiber length over-scaling and under-scaling. As shown in Fig. 6, there is one over-scaling mCC cluster (red) and there are two under-scaling mCC clusters (blue). To extract the binary cortical topography map, a threshold was applied to the group streamline count surface map. (A) The main threshold was defined as the mean + 0.5*STD of the group streamline count value across the entire surface (i.e., Fig. 6C). (B) The threshold was calculated as the mean of the group streamline count value across the entire surface. (C) The threshold was defined as the mean + 1*STD of the group streamline count value across the entire surface. Under each threshold, the differences between the over-scaling and under-scaling clusters of the functional lateralization index, of cortical myelin content, of evolutionary cortical expansion and of developmental cortical expansion are listed on the right side. The comparison showed consistent statistical results with our main text, indicating a limited impact of the cortical mapping threshold on the results.

Supplementary figures

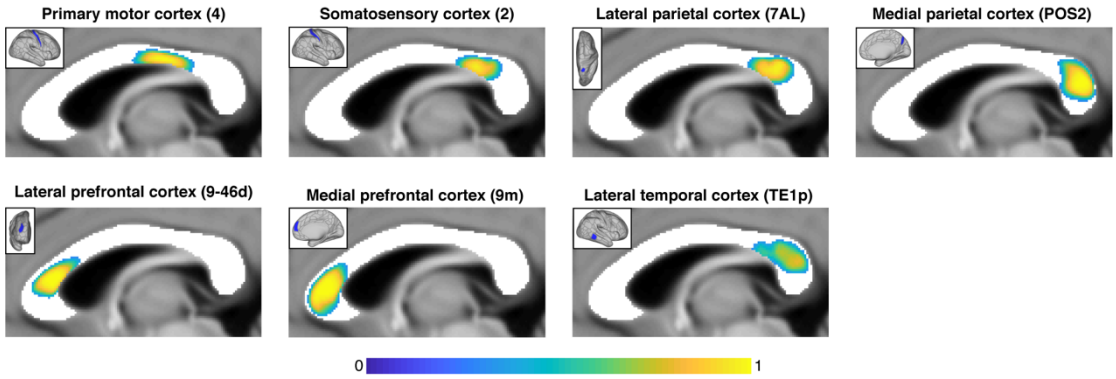

Supplementary Figure 1. Callosal streamlines' passing location on the mCC for selected cortical regions. The resultant group mCC pattern maps are displayed for selected HCPMMP regions on the right hemisphere (blue in solid box): area 4 on the primary motor cortex, area 2 on the somatosensory cortex, area TE1p on the lateral temporal cortex, area 7AL on the lateral parietal cortex, area POS2 on the medial parietal cortex, area 9-46d on the lateral prefrontal cortex, and area 9m on the medial prefrontal cortex. The HCPMMP regional abbreviation is included in the bracket.

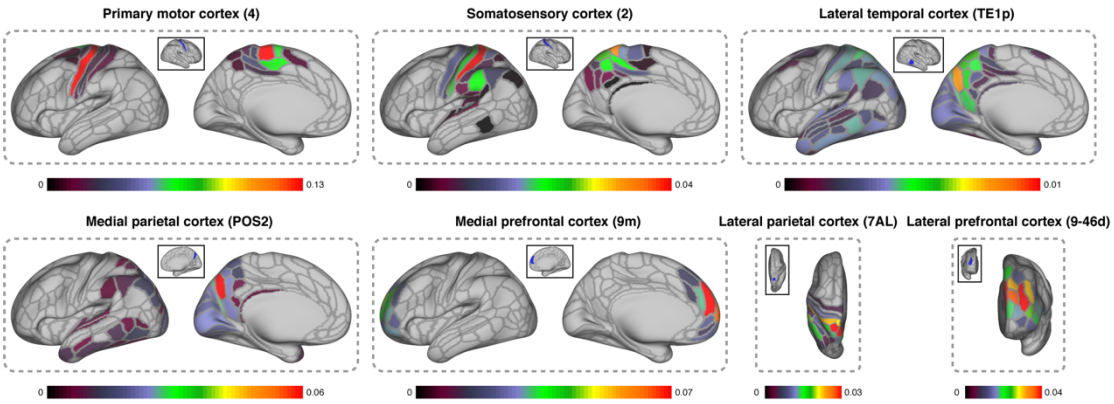

Supplementary Figure 2. Major callosal connections to the contralateral hemisphere for selected cortical regions. For each cortical region, the top strongly connected regions on the contralateral hemisphere are displayed, which together account for at least 80% of total fraction of streamline (FSe) value from this region. The group FSe maps are displayed for selected HCPMMP regions on the right hemisphere (blue in the solid box): area 4 on the primary motor cortex, area 2 on the somatosensory cortex, area TE1p on the lateral temporal cortex, area 7AL on the lateral parietal cortex, area POS2 on the medial parietal cortex, area 9-46d on the lateral prefrontal cortex, and area 9m on the medial prefrontal cortex. The HCPMMP regional abbreviation is included in the bracket. The color bar indicates the FSe value from the selected cortical region.

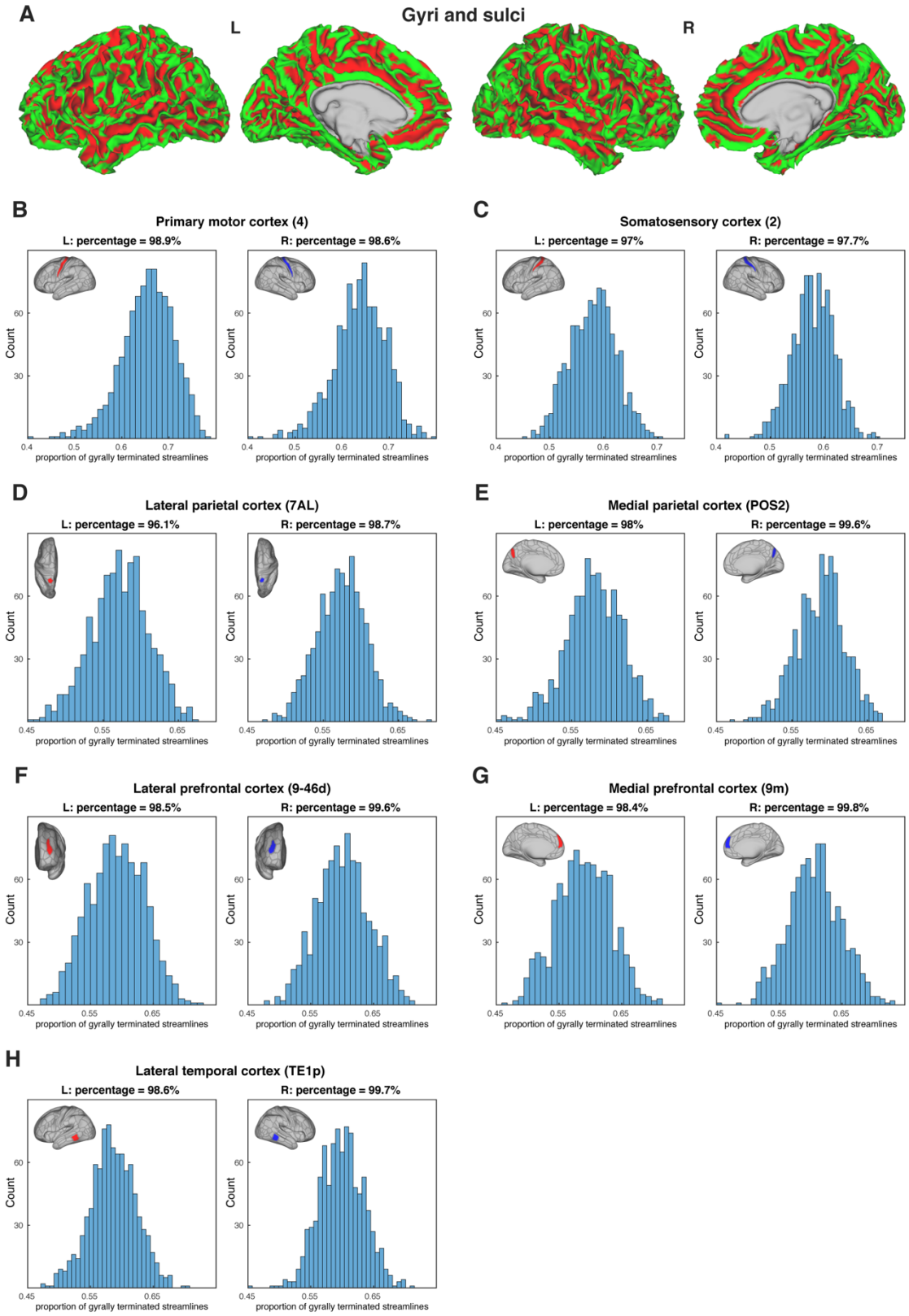
A
Gyri and sulci
L
R
B
Primary motor cortex (4)
L: percentage = 98.9%
R: percentage = 98.6%
C
Somatosensory cortex (2)
L: percentage = 97%
R: percentage = 97.7%
D
Lateral parietal cortex (7AL)
L: percentage = 96.1%
R: percentage = 98.7%
E
Medial parietal cortex (POS2)
L: percentage = 98%
R: percentage = 99.6%
F
Lateral prefrontal cortex (9-46d)
L: percentage = 98.5%
R: percentage = 99.6%
G
Medial prefrontal cortex (9m)
L: percentage = 98.4%
R: percentage = 99.8%
H
Lateral temporal cortex (TE1p)
L: percentage = 98.6%
R: percentage = 99.7%
Count
proportion of gyrally terminated streamlines

840

841 **Supplementary Figure 3. The proportion of gyrally terminated streamlines in the**
842 **contralateral hemisphere for selected cortical regions.** (A) The gyral (green) and sulcal
843 (red) mask from one example subject. The histograms of proportion of gyrally terminated
844 streamlines are displayed for selected HCPMMP regions: (B) area 4 on the primary motor
845 cortex, (C) area 2 on the somatosensory cortex, (D) area 7AL on the lateral parietal cortex,
846 (E) area POS2 on the medial parietal cortex, (F) area 9-46d on the lateral prefrontal cortex,
847 (G) area 9m on the medial prefrontal cortex, and (H) area TE1p on the lateral temporal
848 cortex. Red: cortical region on the left hemisphere; Blue: cortical region on the right
849 hemisphere. The HCPMMP regional abbreviation is included in the bracket.
850

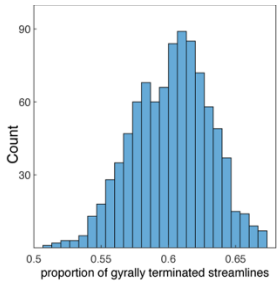

Supplementary Figure 4. The proportion of gyrally terminated streamline for all callosal streamlines.

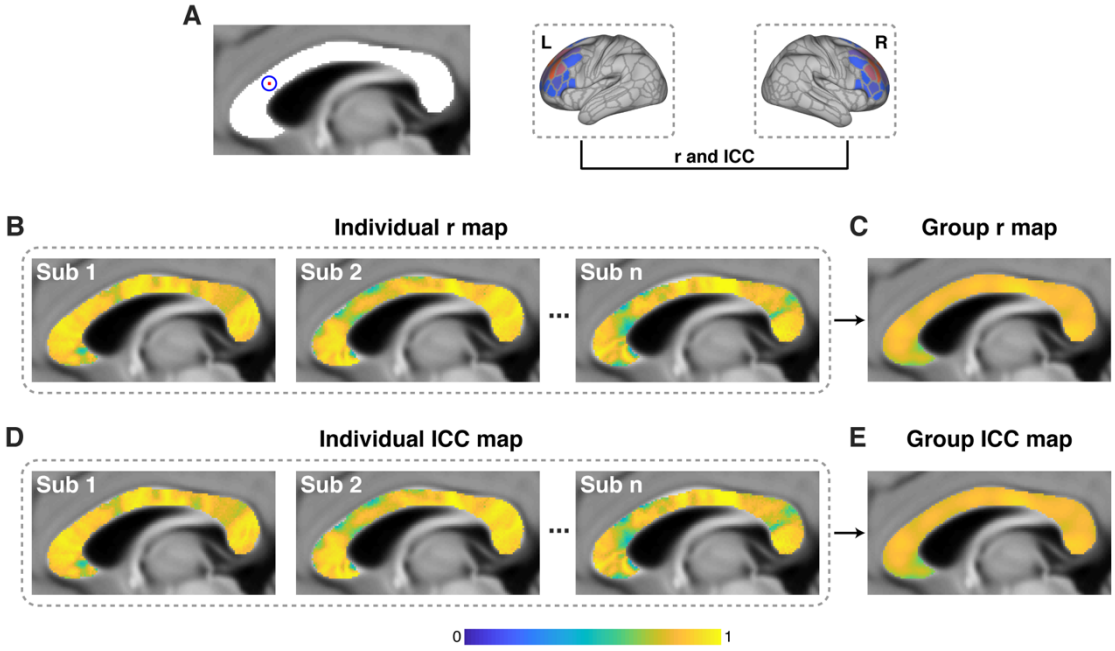

Supplementary Figure 5. Spatial similarity of passing streamline termination pattern between the two hemispheres. (A) Schematic diagram of calculating *r* and *ICC* of termination distribution between left and right hemispheres for one mCC voxel. Individual *r* map (B) and *ICC* map (D) of the mCC. Group *r* map (C) and *ICC* map (E) of the mCC.

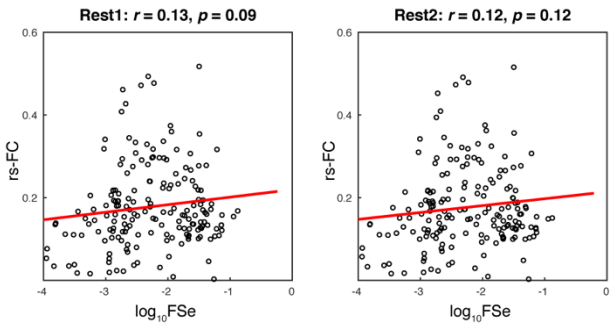

Supplementary Figure 6. Correlation between structural connectivity and functional connectivity. Scatter plots of structural connectivity (FSe) and resting-state functional connectivity (rs-FC, Pearson correlation) across the 180 HCPMMP homotopic regional pairs. Left: Rest1; Right: Rest2.